

## Supporting information

# Multisource vacuum deposition of methylammonium-free perovskite solar cells

*Yu-Hsien Chiang<sup>1</sup>, Miguel Anaya<sup>1</sup>, Samuel D. Stranks<sup>1,2\*</sup>*

<sup>1</sup>Cavendish Laboratory, JJ Thomson Avenue, Cambridge CB3 0HE, United Kingdom

<sup>2</sup>Department of Chemical Engineering & Biotechnology, Philippa Fawcett Drive, Cambridge CB3 0AS, United Kingdom

### **Methods:**

#### *Perovskite film evaporation*

The substrates were cleaned with soap, deionized water, acetone and isopropanol in a sonication bath for 15 minutes at each step. After that, the clean substrates were treated by UV-Ozone for 15 minutes. The deposition process took place in a chamber installed in a N<sub>2</sub>-filled glovebox to avoid exposure of precursors and deposited films to oxygen and water during sample fabrication and handling. The clean substrates were transferred to a CreaPhys PEROVap evaporator inside an MBraun N<sub>2</sub> glovebox (O<sub>2</sub> and H<sub>2</sub>O levels below 0.5 ppm). The chamber was pumped down to a pressure of 1-3x10<sup>-6</sup> mbar for the deposition. We employed a specifically designed cooling system that maintains the evaporator walls, source shutters and shields at -20°C throughout the entire process. This functionality minimizes re-evaporation of the precursors and cross-contamination between sources, ensuring fine control over the evaporation rates and high reproducibility. For mixed cation lead mixed halide deposition, FAI (GreatCell

Solar), lead iodide (TCI or Lumtec with >98% and >99.999% metal trace based purity, respectively; we used TCI for all experiments unless stated otherwise) and Cesium bromide (Sigma) were filled into three different crucibles. For the organic cation, we used fresh FAI powder for every deposition. The tooling factor of each chemical was calibrated by checking the film thicknesses by profilometry inside the N<sub>2</sub>-filled glovebox (DEKTAK XT profilometer). Five quartz crystal microbalances (QCMs) mounted on the top of vapor sources allows us to monitor the deposition rate of each source and control the composition. We set the rate of FAI and CsBr at 1 Å/s and 0.1 Å/s, respectively, and vary the PbI<sub>2</sub> rate from 0.7-0.9 Å/s to change the perovskite composition. The substrate temperature was maintained at around 18°C. The distance between evaporator sources and substrate holder is around 35 cm. We observed minimal change in the substrate temperature (<1°C), and the chamber was typically at a pressure of 1-4x10<sup>-6</sup> mbar during deposition. See Table S1 for evaporation parameters.

### *Device fabrication*

ITO (150 nm) coated glass substrates were cleaned and UV-Ozone treated following the procedures described above. To prepare the transporting layer, the substrates were transferred into an N<sub>2</sub>-filled MBraun glovebox (O<sub>2</sub> and H<sub>2</sub>O levels below 0.5 ppm). All the spin-coating conditions were optimised for the spin-coater integrated inside the glovebox. For the bottom hole transporting layer, we prepared PTAA (Sigma) solution with a concentration of 2 mg/ml in anhydrous toluene (Sigma) and stirred the solution overnight. To spin the PTAA, we dropped the solution on the substrate and spin-coated it at 5000 rpm (1000 rpm/s ramp) for 30 seconds with the spin-coater lid closed. After the perovskite deposition, we annealed the film at 135°C for different times to optimize the device performance. The best performance device was achieved with 90 mins annealing time. After the film cooled down to room temperature, PCBM

(Merck) (20 mg/ml in anhydrous Chlorobenzene, sigma) was spin-coated dynamically on the perovskite film at 1200 rpm for 30 seconds with the lid open. The film was dried at room temperature in the glovebox for 20 minutes. The buffer layer, Bathocuproine (BCP; Alfa Aesar), was spin-coated dynamically on PCBM at 2000 rpm for 30 seconds. Finally, we evaporated 100 nm of Ag at 1 Å/s to complete a full device in the same evaporator system that we employed to deposit the perovskite films.

### *Solution-processed perovskite film preparation*

To understand the composition of evaporated perovskite films, we solution-processed a series of films with the composition of  $\text{FA}_{1-x}\text{Cs}_x\text{Pb}(\text{I}_{1-y}\text{Br}_y)_3$ , where  $x$  and  $y$  are varied from 0.1 to 0.46. The precursor stoichiometry determines the composition here. A 1 M precursor solution was made by dissolving FAI,  $\text{PbI}_2$ , CsI and  $\text{PbBr}_2$  in DMF/DMSO (4:1). Before the spin-coating process, we purged the  $\text{N}_2$ -filled glovebox for 15 minutes to achieve a clean atmosphere. To fabricate the films, 50  $\mu\text{l}$  of perovskite precursor solution was deposited on a clean glass substrate (see cleaning procedure above) and spin-coated at 1000 rpm for 10 s and 6000 rpm for 20 s. At 5 seconds before the end of the second spinning step, we dropped 100  $\mu\text{l}$  of chlorobenzene on the middle of the substrate (antisolvent method). After the spinning process, the perovskite films were immediately moved to a hotplate and were annealed at 100°C for 30 minutes. The spin-coating process is optimized for an integrated spin-coater in an MBraun glovebox with the lid open.

### *Scanning electron microscopy (SEM)*

Film morphology was imaged by employing a field-emission scanning electron microscope (LEO GEMINI 1530VP FEG-SEM) with an electron beam energy of 3 kV and an in-lens detector in secondary electron detection mode.

### *X-ray diffraction (XRD) pattern measurements*

We used a Bruker D8 ADVANCE system with a Copper focus X-ray tube (K $\alpha$ : 1.54 Å) to obtain the XRD patterns of the films of study. The scan range for  $2\theta$  was from 5° to 40° with a step size of 0.01° and a delay time of 0.15 s. To study the film properties, we loaded the perovskite film into an air-tight sample holder inside the glovebox to avoid air exposure. For the moisture stability test, the perovskite samples were stored in air with a relative humidity of ~50%. For the air stability test, we kept the perovskite film in a dry box with a relative humidity of <10%. The structural analysis was carried out in the TOPAS 5 software where we ran an indexing fitting procedure to determine the possible space groups. A Pawley refinement was used to check these space groups and obtain the space group based on the best fits.

### *UV-Vis measurements*

UV-Vis transmittance spectra were collected on an Agilent 8453 UV-vis spectrophotometer by using a tungsten (310–1100 nm) lamp for illumination. The system is equipped with a photodiode array for detection.

### *Photoluminescence quantum efficiency (PLQE) measurements*

PLQE measurements were conducted by exciting the samples with a 520 nm-continuous wave laser. We set the excitation power density at 60 mW/cm<sup>2</sup> (1-sun equivalent intensity) by using a calibrated power meter. The PLQE measurement and calculation protocol are based on the de Mello paper.<sup>1</sup> For this, we take three measurements: background signal, laser on the sample and laser off the sample. The sample was mounted in an integrating sphere to collect all the PL by an optical fibre coupled to an Andor iDus Si Detector. The accumulation time for each measurement is 30 seconds. The quasi Fermi level splitting values were obtained by making use of the equation  $V_{oc} \approx V_{oc,rad} + \frac{KT}{e} \ln(PLQE)$ . All the samples were encapsulated in the N<sub>2</sub>-filled glovebox.

### *Time-correlated single-photon counting (TCSPC) measurements*

TCSPC measurements were conducted using a 407-nm pulsed laser diode (PicoQuant) with a function generator for excitation and collecting the signal by a microchannel plate - photomultiplier tubes detector. Two long pass filters at 420 nm and 470 nm were used to avoid the laser signal from reaching the detector. The time-resolved PL fluences were set to be around one sun illumination, with a repetition rate of 0.5 MHz and a pulse fluence of ~5 nJ/pulse/cm<sup>2</sup>

### *Hyperspectral PL measurements*

Hyperspectral PL measurements were acquired using a widefield microscope (IMA VIS™, Photon Etc.) equipped with a 1040 × 1392 resolution silicon CCD camera. We excited the films with a 405 nm, continuous wave laser, and obtained the PL maps in reflectance mode with a 100x (0.9 NA) objective. We employed a tunable Bragg filter to obtain the spectrally resolved

maps from 700 nm to 850 nm with a step size of 2 nm. The excitation power density was calibrated with a power meter to be 60 mW/cm<sup>2</sup> (one sun equivalent intensity).

### *J-V scans*

We performed current-voltage (J-V) curve measurements with illumination from a xenon lamp (Abet Sun 2000 Solar Simulators, AAB class) with 1 sun intensity (100 mW/cm<sup>2</sup>, AM 1.5G), calibrated with a reference Silicon diode. The device performance was recorded with a source meter, Keithley 2636A, controlled by a LabVIEW program. The J-V curve is obtained by scanning from 1.2 to -0.1 V (reverse scan) and -0.1 to 1.2 V (forward scan) with a step size of 20 mV and a delay time of 100 ms. The solar cells active area is 15.5 mm<sup>2</sup>, defined by the overlapping area between Ag and ITO. All the devices were encapsulated in the N<sub>2</sub>-filled glovebox before the measurement.

### *External quantum efficiency (EQE) measurements*

To obtain the EQE spectra of the devices, we used a Bentham PVE300 system equipped with xenon-quartz and tungsten halogen lamps, and a single monochromator (Bentham TMc 300). During the measurement, we used a transformer mode (Bentham S400 474) with a frequency of 600 Hz and a signal detection unit (Bentham S400 417) to measure the spectral response and EQE of the evaporated perovskite solar cells. EQE measurements were taken 30 days after JV curves were obtained. A silicon reference cell was used to calibrate the spectral mismatch. The response of the solar cells was obtained for a spectral range covering from 300 to 900 nm with a step size of 5 nm. EQE and JV curves of devices measured at comparable device age show good agreement.

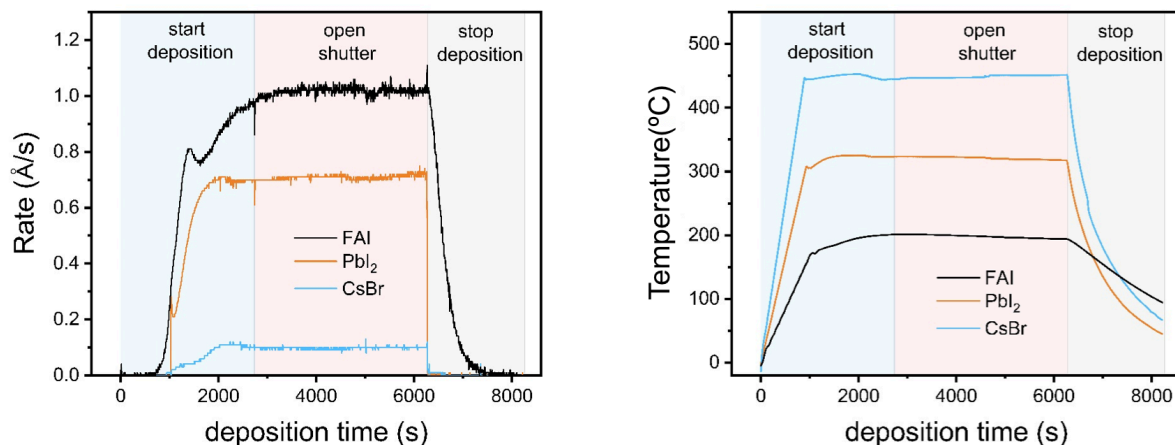


Figure S1. Parameters of a multi-sourced evaporation process for a typical batch of a control film  $\text{FA}_{0.7}\text{Cs}_{0.3}\text{Pb}(\text{I}_{0.9}\text{Br}_{0.1})_3$ , showing the deposition rate (left panel) and sublimed temperature (right panel) of FAI,  $\text{PbI}_2$  and CsBr.

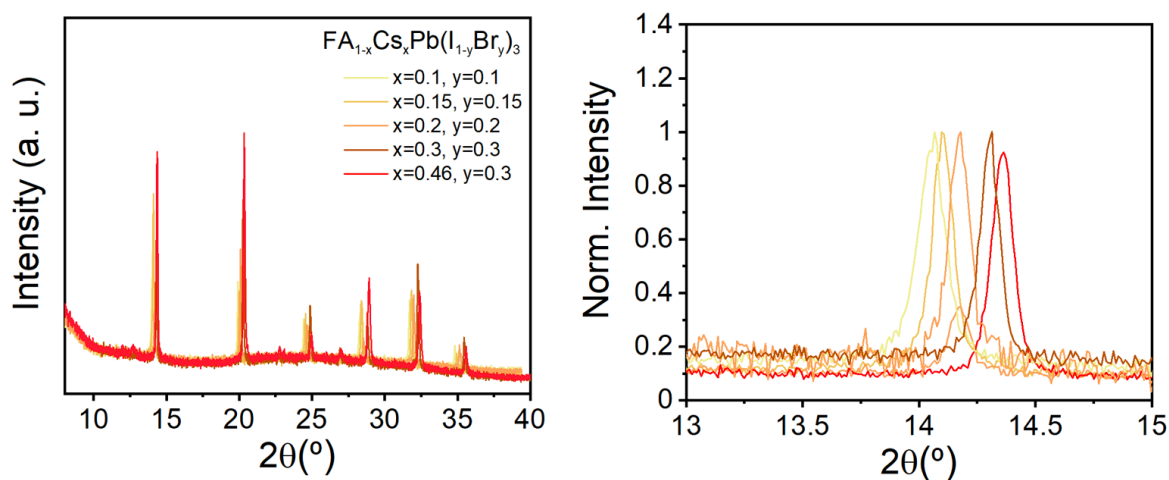


Figure S2. XRD patterns of a series of solution-processed films with  $\text{FA}_{1-x}\text{Cs}_x\text{Pb}(\text{I}_{1-y}\text{Br}_y)_3$  composition, where  $x$  and  $y$  take a range of values between 0.1 – 0.46. The right panel shows a zoom around the key perovskite peaks used in the analysis in Figure S3.

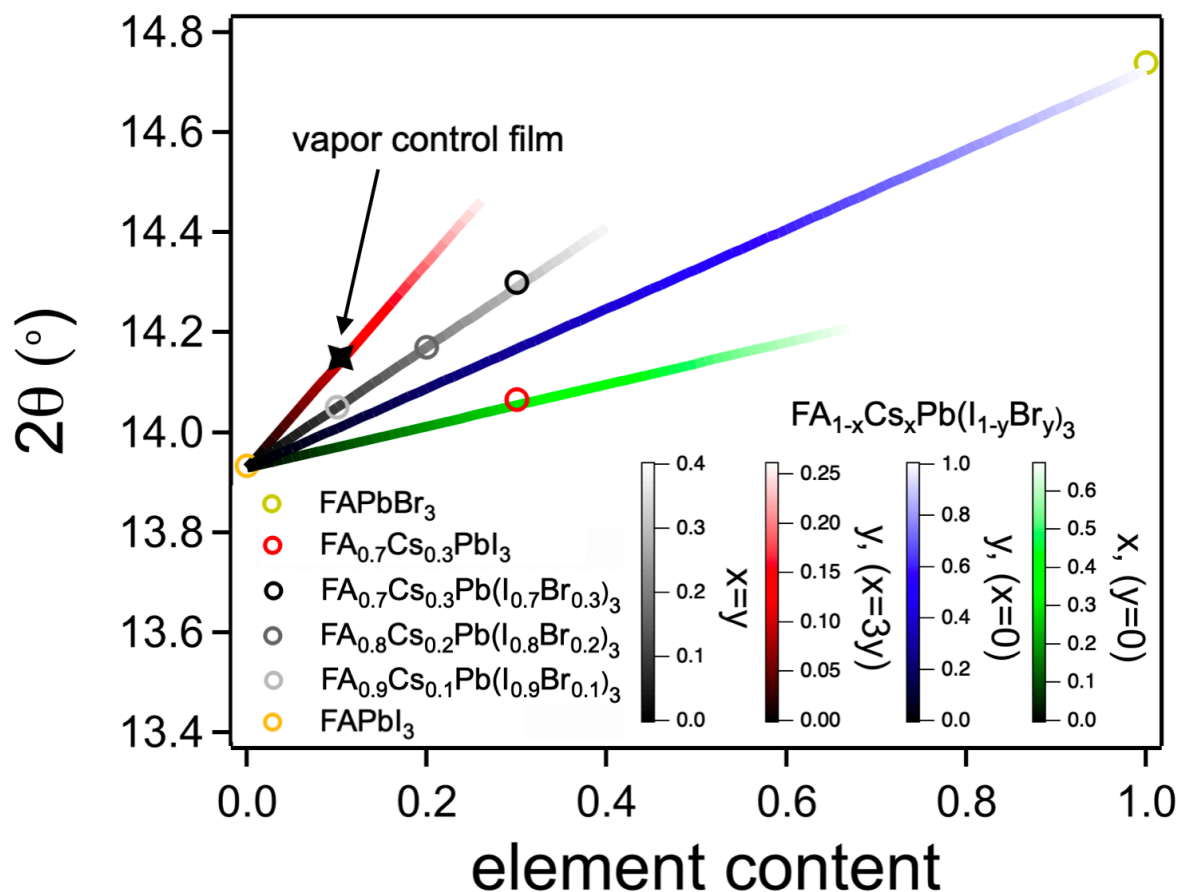


Figure S3. Plot used to estimate the final composition of the evaporated film. We solution-processed a series of perovskite films with different Cs and Br fractions and characterized their bulk properties by extracting peak positions of the perovskite XRD peaks (Figure S2). We estimate the stoichiometry of the solution-processed films by considering the concentration of A and X components in the precursor solutions<sup>2,3</sup>. By assuming Vegard's law for composition ranges which maintain the same phase, we estimate the evolution of the perovskite peak in the: i)  $\text{FA}_{1-x}\text{Cs}_x\text{PbI}_3$  (green curve), ii)  $\text{FAPb}(\text{I}_{1-y}\text{Br}_y)_3$  (blue curve) and iii)  $\text{FA}_{1-x}\text{Cs}_x\text{Pb}(\text{I}_{1-y}\text{Br}_y)_3$  (black curve) perovskite families. Specifically, we use the XRD peaks from the  $\text{FA}_{0.7}\text{Cs}_{0.3}\text{Pb}(\text{I}_{0.7}\text{Br}_{0.3})_3$  and  $\text{FA}_{0.54}\text{Cs}_{0.46}\text{Pb}(\text{I}_{0.7}\text{Br}_{0.3})_3$  films to determine the specific influence of Cs on the lattice parameter, hence determining the slope of the green curve. We note that the green line is only plotted up to  $x = 0.67$  in order to maintain the cubic perovskite phase, thus avoiding phase transitions.<sup>4</sup> We determine the slope of the blue curve by considering experimental XRD peaks of the films in which we change the Br fraction, i.e.  $\text{FA}_{0.9}\text{Cs}_{0.1}\text{Pb}(\text{I}_{0.9}\text{Br}_{0.1})_3$  and  $\text{FA}_{0.3}\text{Cs}_{0.7}\text{Pb}(\text{I}_{0.3}\text{Br}_{0.7})_3$ , and we decouple the influence of Cs using the blue line dependence; this isolates the effect of Br on the lattice parameter, i.e. the  $\text{FAPb}(\text{I}_{1-y}\text{Br}_y)_3$  family. By knowing the specific influence of Cs and Br on the lattice parameter, we can thus generate the line corresponding to  $\text{FA}_{1-x}\text{Cs}_x\text{Pb}(\text{I}_{1-y}\text{Br}_y)_3$  (black curve). These plots match our experimental data (gray circles) and those values reported for  $\text{FA}_{0.7}\text{Cs}_{0.3}\text{PbI}_3$ ,  $\text{FAPbBr}_3$  and  $\text{FAPbI}_3$  in the literature<sup>5-7</sup> (colored circles), validating the approach. We apply this methodology to estimate the composition of our evaporated perovskite by assuming that Cs:Br ratio is kept to 1:1, in line with the source of Cs and Br being CsBr. Therefore, we predict the lattice constant calibration curve of



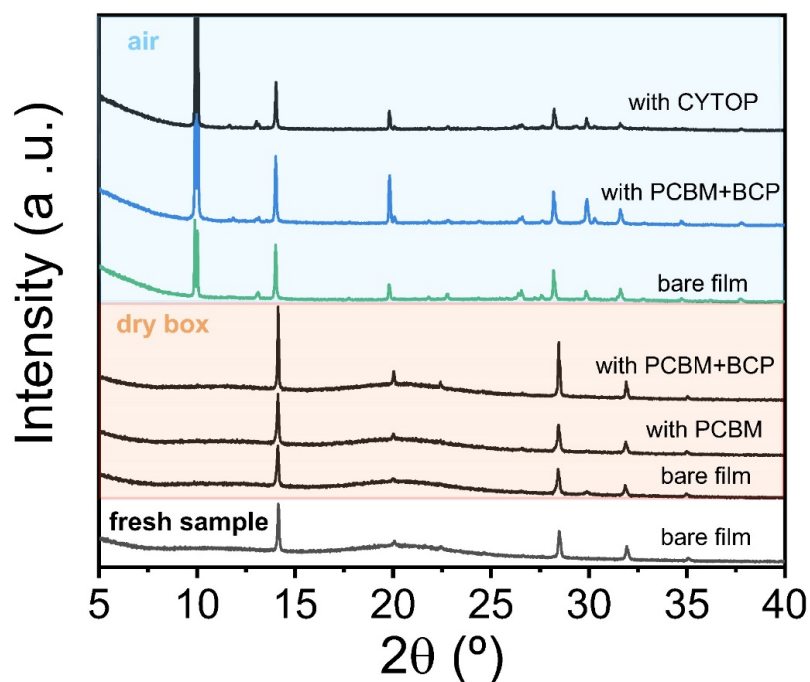


Figure S5. The structure stability test by XRD with evaporated perovskite films coated with different contact layers on top. CYTOP is an amorphous fluoropolymer with low moisture and air permeability ( $<10^{-12}$  cm<sup>3</sup>.cm/(cm<sup>2</sup>s Pa)). The “air” and “dry box” labels in the figure indicate when the samples were stored in an atmosphere with a relative humidity of  $50 \pm 5\%$  and  $<10\%$ , respectively. To avoid moisture degradation, the fresh and “dry box” samples were kept in an air-tight sample holder during the XRD measurement.

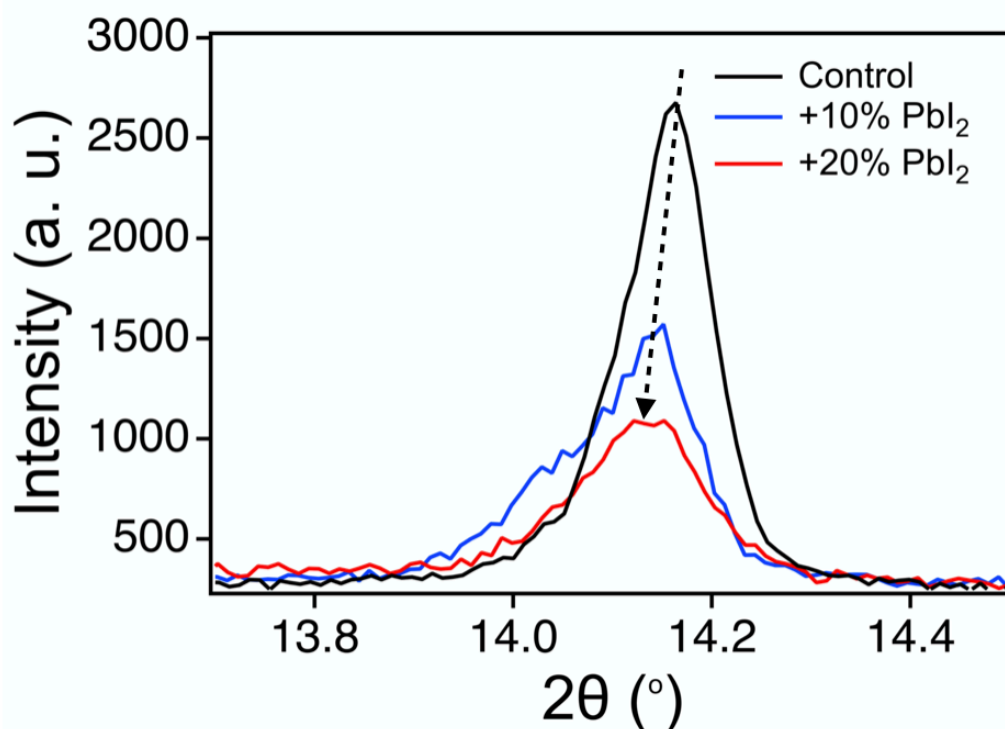


Figure S6. Zoom-in XRD of the (011) perovskite peak from Figure 2a-c.

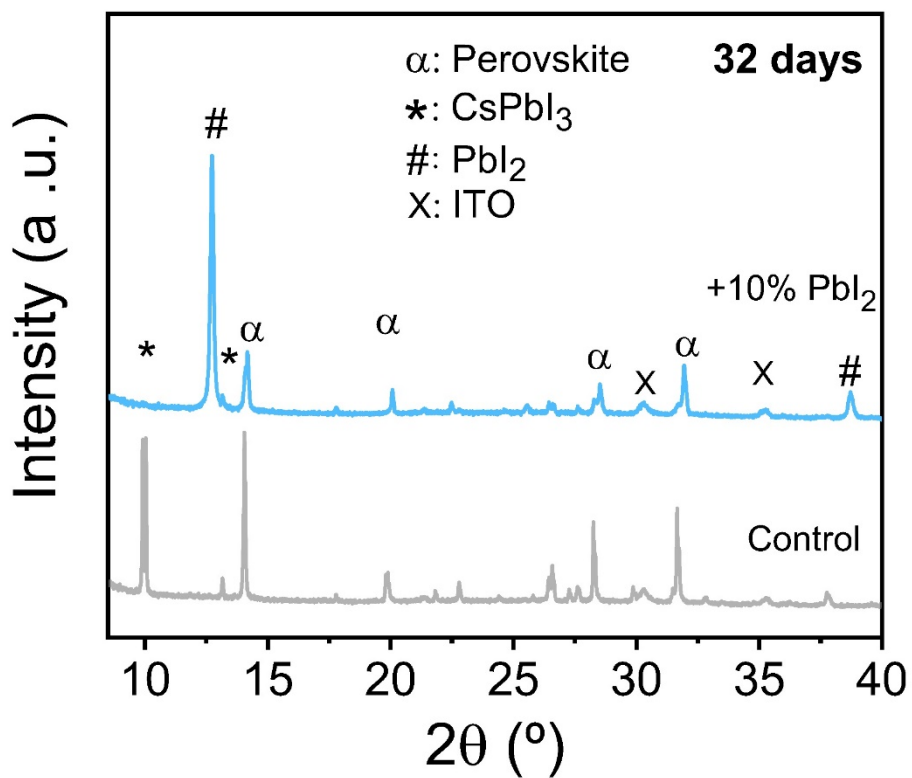


Figure S7. The air stability test of control and +10% PbI<sub>2</sub> perovskite film deposited on PTAA/ITO substrate, stored in ambient air for 32 days (relative humidity 50 ± 5%).

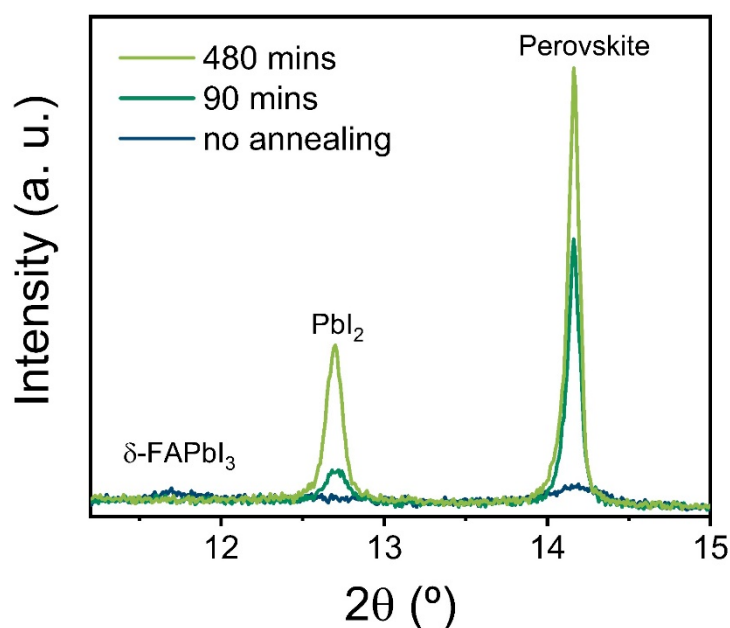


Figure S8. XRD patterns of evaporated perovskite films under thermal stress. We annealed the perovskite film inside the glovebox at 135°C for 90 and 480 minutes. The XRD pattern for the non-annealed film is also shown for comparison.

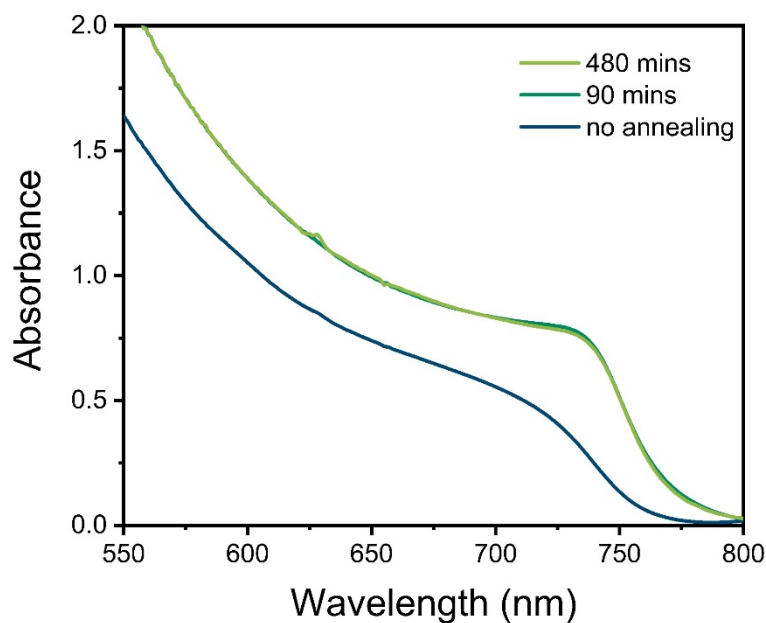


Figure S9 UV-Vis spectra of evaporated perovskite films with different heat treatments. We annealed the perovskite films inside an N<sub>2</sub>-filled glovebox at 135°C for 90 and 480 minutes, showing a negligible absorption change. The UV-Vis spectrum for the non-annealed film is also shown for comparison.

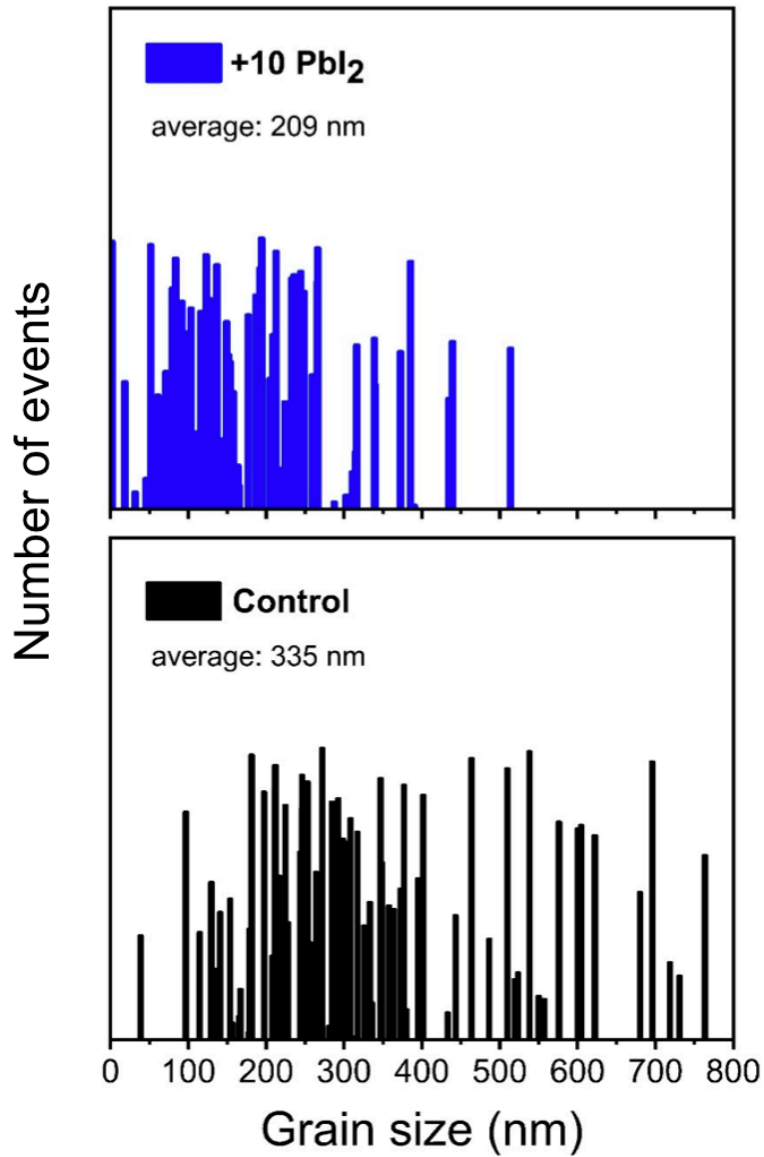


Figure S10. The grain size distribution of perovskite films with control and +10 PbI<sub>2</sub> perovskite film on PTAA/ITO substrate. The grain size was obtained by calculating the square-root of the grain area estimated using the software ImageJ.

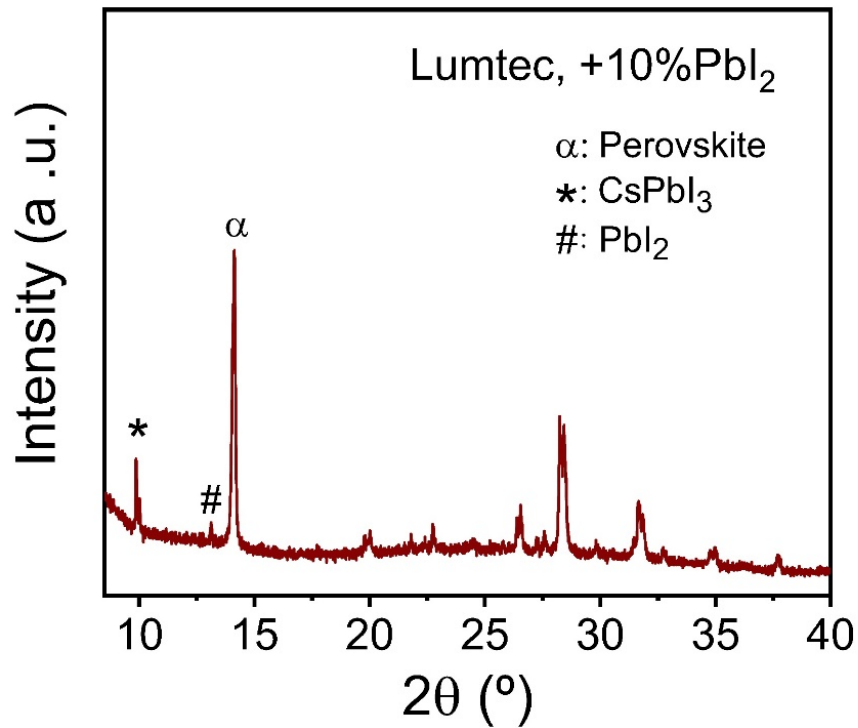


Figure S11. XRD pattern of a +10% PbI<sub>2</sub> evaporated perovskite film by using Lumtec PbI<sub>2</sub> as a precursor (see Methods section above for more details), highlighting the sensitivity to the PbI<sub>2</sub> source and the deposition process in the final characteristics of the perovskite. The XRD data was measured in air, and we saw degradation of the film after 15 mins, with the appearance of a CsPbI<sub>3</sub> peak.

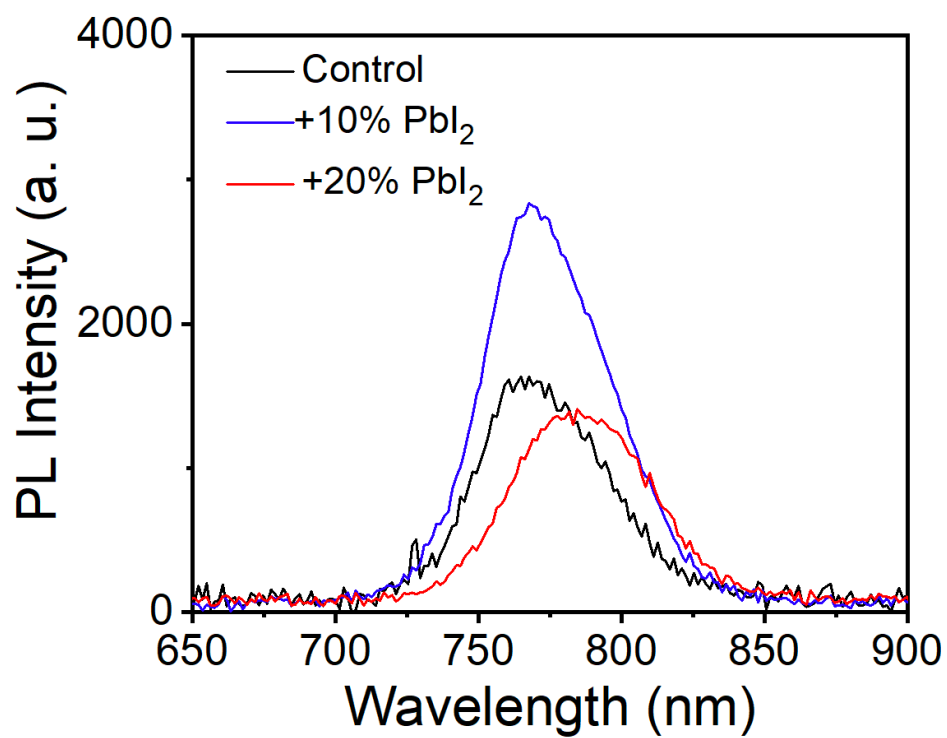


Figure S12. Unnormalized PL spectra (excitation at 520 nm) of evaporated perovskite with different excess of PbI<sub>2</sub>.

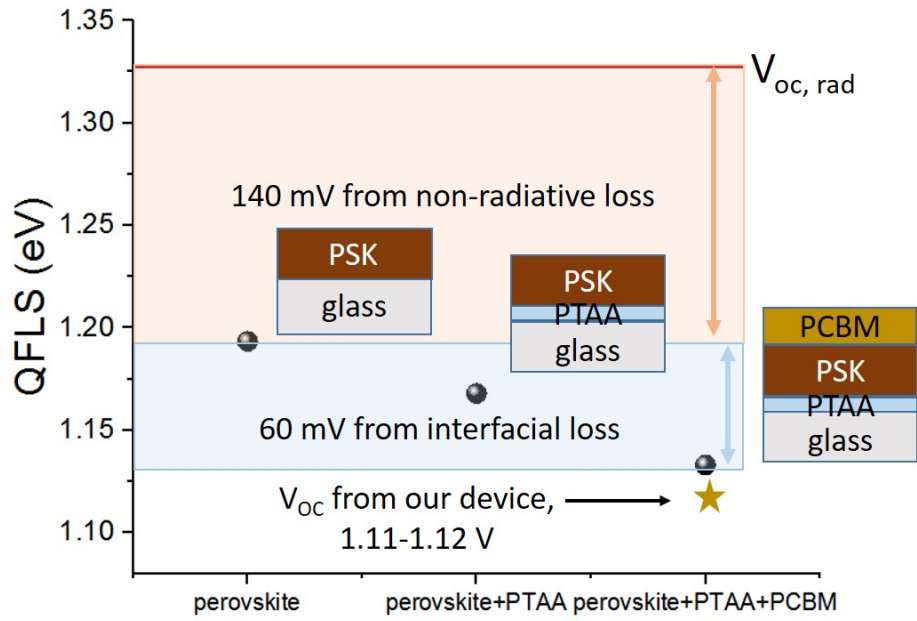


Figure S13. The quasi-fermi level splitting for the perovskite (10% sample) with n-type and p-type transporting layers, calculated from the PLQE results. The black and star symbols are based on film PLQE and device  $V_{oc}$  measurements (10%  $PbI_2$  device), respectively.

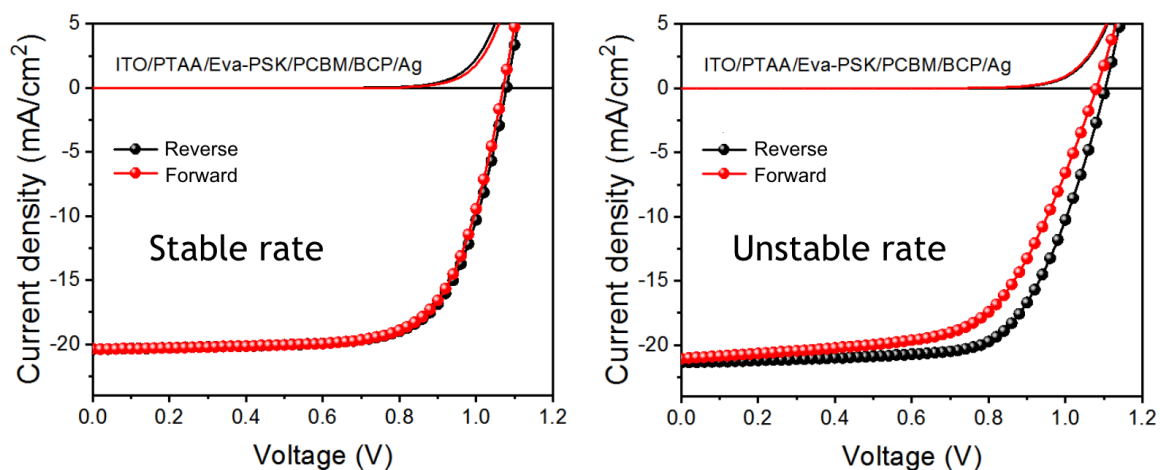


Figure S14. J-V curves for evaporated perovskite solar cells (+10%  $\text{PbI}_2$ ) deposited with a stable (left panel) and unstable (right panel) rate. A more pronounced hysteresis effect can be seen in the device with an unstable rate during the film deposition.

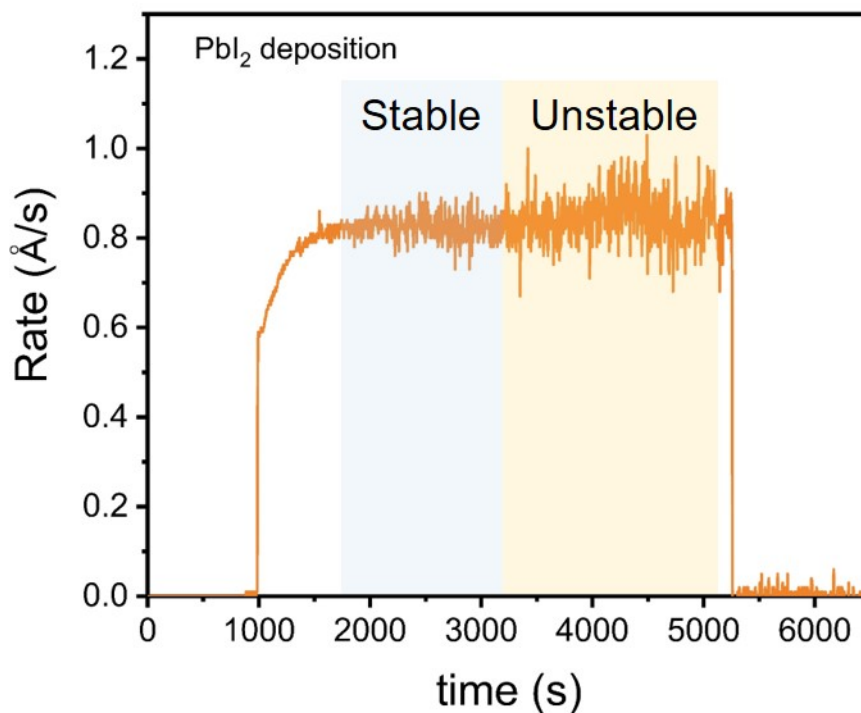


Figure S15. Variation in  $\text{PbI}_2$  rate during an unstable perovskite evaporation batch. See Figure S1 for an example of a stable rate.

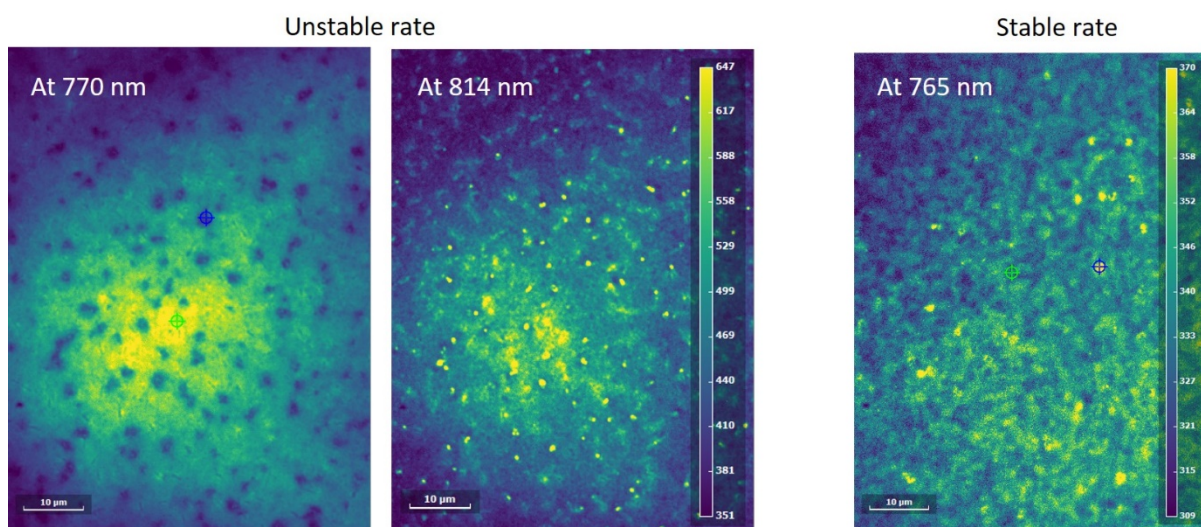


Figure S16. Hyperspectral photoluminescence (PL) maps of evaporated perovskite films (+10% excess  $\text{PbI}_2$ ) on glass. The left and middle maps correspond to a sample obtained with an unstable deposition rate (see Figure S15). The PL peak distributions are spatially and spectrally inhomogeneous, showing maxima at 770 and 814 nm, which is indicative of phase segregation. The right map is the PL signal from a film obtained with a stable deposition rate, showing a single peak emission spectrum with its maximum at 765 nm.

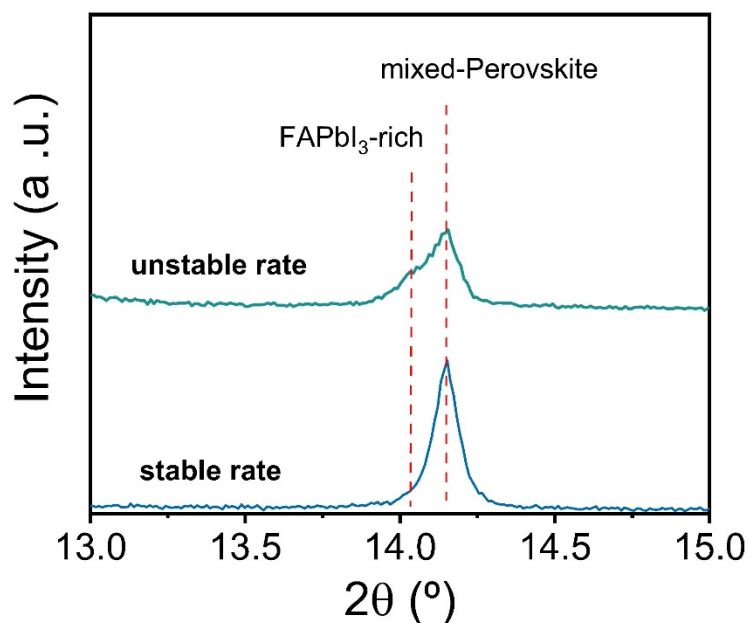


Figure S17. XRD patterns to understand the structure of the perovskite film (10% excess PbI<sub>2</sub>) deposited with stable and unstable rates. When the evaporation rate is unstable (see Figure S15), we observe an asymmetric perovskite peak with a shoulder at lower  $2\theta$ , corresponding to FAPbI<sub>3</sub>-rich domains.<sup>9</sup> For the perovskite film deposited with a stable rate, there is negligible asymmetry in the XRD peak (blue curve).

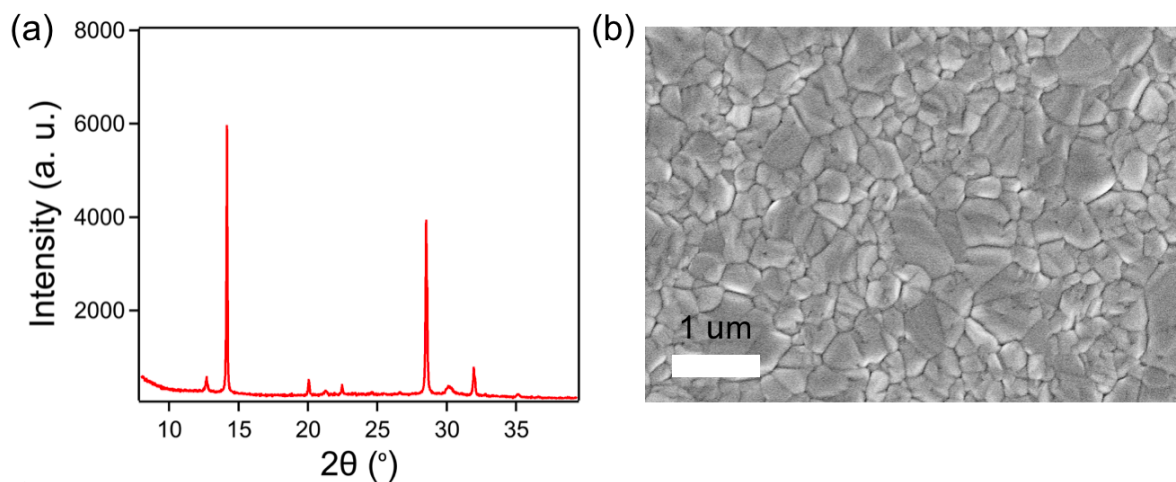


Figure S18. The structural and morphological characterization of the evaporated perovskite film with 5% excess PbI<sub>2</sub> deposited on a PTAA/ITO substrate. (a) XRD pattern and (b) top-view SEM image of the film.

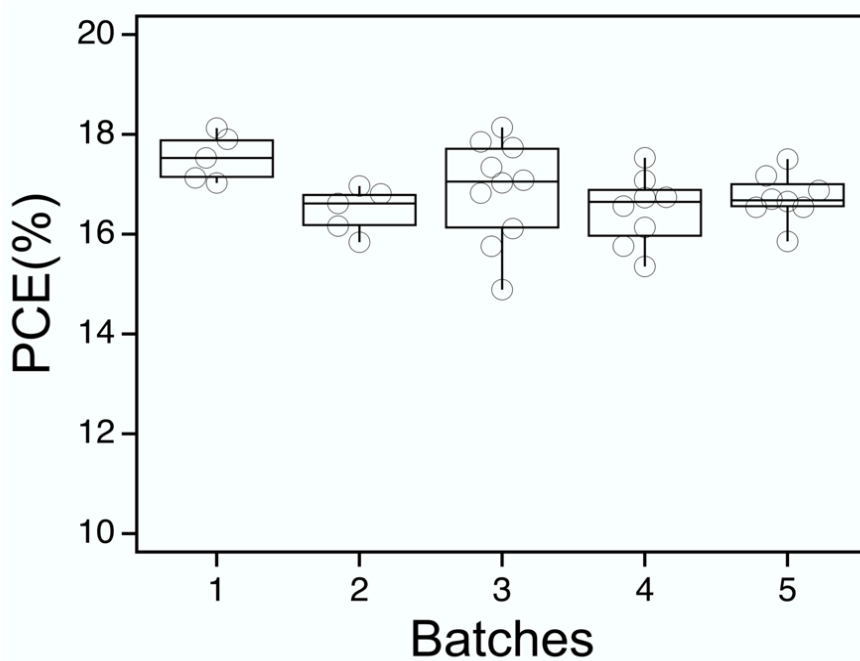


Figure S19. Device performance for 5%  $\text{PbI}_2$  excess evaporated perovskite solar cells from reverse scan measurement of J-V scan under 1 sun AM 1.5G illumination across five different batches.

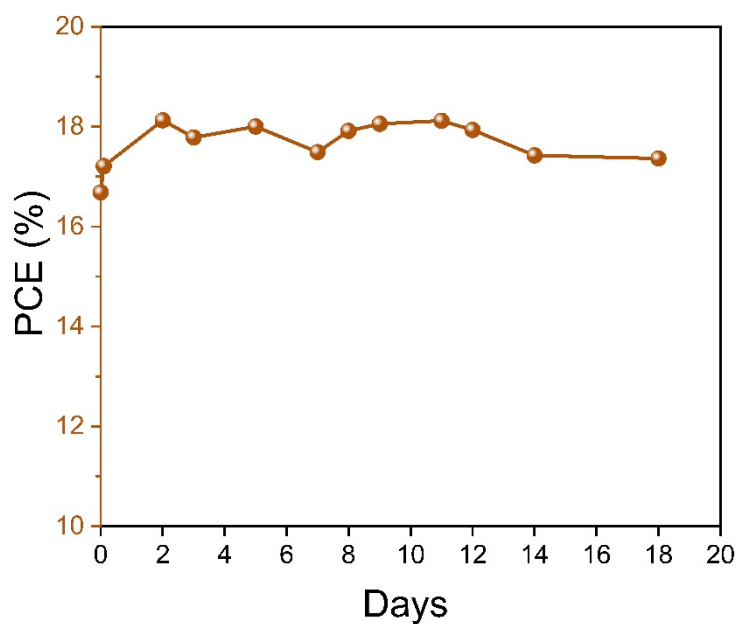


Figure S20. The shelf-stability test of an encapsulated device measured over a period of 18 days, with the devices stored and measured in air. The J-V measurements are under 1 sun AM 1.5G illumination. The PCE here is the value from the reverse scan of the J-V curve.

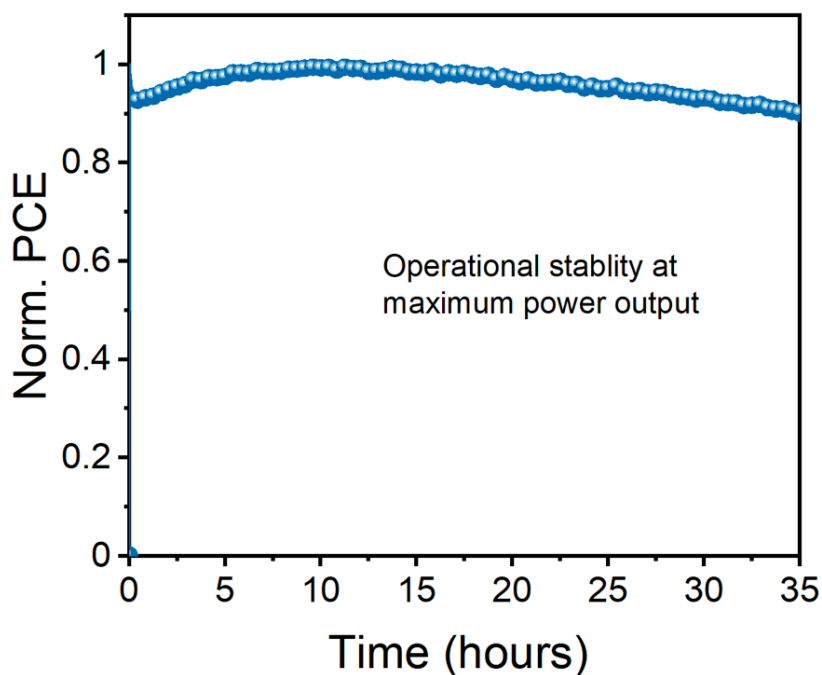


Figure S21. Operational stability test of encapsulated solar cells in air under AM 1.5 G 1-sun intensity light at maximum power point based on the initial reverse scan (0.8 V). We note there is no UV filter.

Table S1. Parameters for the substrate rotation speed and the evaporation conditions for the different precursors employed for the optimized (5% excess  $\text{PbI}_2$ ) perovskite films. We note that the Z-factor was set to 1 for both FAI and  $\text{PbI}_2$ .

	FAI	$\text{PbI}_2$	CsBr	substrate
Z-factor	1	1	1.41	
Tooling factor (%)	40	36.1	25	
Density ( $\text{g}/\text{cm}^3$ )	2.22	6.16	4.52	
Rate ( $\text{\AA}/\text{s}$ )	1	0.7	0.1	
Speed (rpm)				11

## References:

1. de Mello, J. C.; Wittmann, H. F.; Friend, R. H. An Improved Experimental Determination of External Photoluminescence Quantum Efficiency *Adv. Mater.*, **1997**, *9*, 230–232.
2. Turren-Cruz, S.-H.; Hagfeldt, A.; Saliba, M. Methylammonium-Free, High-Performance, and Stable Perovskite Solar Cells on a Planar Architecture *Science* **2018**, *362*, 449.
3. Gao, X.-X.; Yi, W. L.; Hu, Z. R.; Zhang, B.; Züttel, A.; Feng, Y.; Nazeeruddin, M. K. Stable and High-Efficiency Methylammonium-Free Perovskite Solar Cells *Adv. Mater.* **2020**, *32*, 1905502
4. Schelhas, L. T.; Li, Z.; Christians, J. A.; Goyal, A.; Kairys, P.; Harvey, S. P.; Kim, D. H.; Stone, K. H.; Luther, J. M.; Zhu, K.; Stevanovice, V.; Berry, J. J. Insights into Operational Stability and Processing of Halide Perovskite Active Layers *Energy Environ. Sci.*, **2019**, *12*, 1341-1348.
5. Yu, Y.; Wang, C.; Grice, C. R.; Shrestha, N.; Chen, J.; Zhao, D.; Liao, W; Cimaroli, A. J.; Roland, P. J.; Ellingson, R. J.; Yan, Y. Improving the Performance of Formamidinium and Cesium Lead Triiodide Perovskite Solar Cells using Lead Thiocyanate Additives *ChemSusChem* **2016**, *9*, 3288-3297.
6. Subbiah, A. S.; Agarwal, S.; Mahuli, N.; Nair, P.; Hest, M. V.; Sarkar, S. K. Stable p–i–n FAPbBr<sub>3</sub> Devices with Improved Efficiency Using Sputtered ZnO as Electron Transport Layer. *Adv. Mater. Interfaces*, **2017**, 1601143
7. Yuan, D.-X.; Gork, A.; Xu, M.-F. Wang, Z.-K.; Liao, L.-S. Inverted Planar NH<sub>2</sub>CHNH<sub>2</sub>PbI<sub>3</sub> Perovskite Solar Cells with 13.56% Efficiency via Low Temperature Processing *Phys. Chem. Chem. Phys.*, **2015**, *17*, 19745.
8. Holliman, P. J.; Jones, E. W.; Hobbs, R. J.; Connell, A.; Furnell, L.; Anthony, R.; Ker-shaw, C. P. Quantitative chemical analysis of perovskite deposition using spin coating *Mater. Letters: X*, **2019**, *2*, 100011.
9. Eperon, G. E.; Stranks, S. D.; Menelaou, C.; Johnston, M. B.; Herz, L. M.; Snaith, H. J. Formamidinium Lead Trihalide: A Broadly Tunable Perovskite for Efficient Planar Heterojunction Solar Cells *Energy Environ. Sci.*, **2014**, *7*, 982–988.